CHALMERS
UNIVERSITY OF TECHNOLOGY

Vehicle Motion Control Allocation Including Tire Wear Minimization

Citation for the original published paper (version of record):
Ghandriz, T., Janardhanan, S. (2026). Vehicle Motion Control Allocation Including Tire Wear Minimization. IEEE Open Journal of Vehicular Technology, 7: 901-916.
http://dx.doi.org/10.1109/OJVT.2026.3666361

(article starts on next page)

IEEE Open Journal of Vehicular Technology

Received 10 February 2026; accepted 17 February 2026. Date of publication 19 February 2026;
date of current version 18 March 2026. The review of this article was coordinated by Editor Lei Zhang.

Digital Object Identifier 10.1109/OJVT.2026.3666361

Vehicle Motion Control Allocation Including Tire Wear Minimization

TOHEED GHANDRIZ [1,2] AND SACHIN JANARDHANAN [1,2]

[1] Volvo Group Trucks Technology, 417 15 Gothenburg, Sweden
[2] Chalmers University of Technology, 412 96 Gothenburg, Sweden

CORRESPONDING AUTHOR: TOHEED GHANDRIZ (e-mail: toheed.ghandriz@chalmers.se).

This work was supported by Swedish Energy Agency and Volvo Group Truck Technology.

ABSTRACT Tire wear is a major source of microplastic emissions, adversely affecting soil, water, air quality, and ecosystems, while also representing a non-negligible operational cost for road vehicles. This paper proposes a unified, monetary-cost-based control allocation framework for distributed-drive electric vehicles that jointly minimizes electric energy consumption and tire wear. Both objectives are expressed in a common economic unit (e.g., cost rate per time or distance), enabling explicit and transparent trade-offs between propulsion efficiency and tire wear within a single optimization problem. A mixed-integer, optimization-based control allocation strategy is developed to distribute wheel forces and motor torques across multiple axles and wheels, implicitly managing tire slip while prioritizing actuators based on both electrical efficiency and wear-related economic costs. To enable wear-aware control, an empirical tire wear model is introduced that accounts for longitudinal and lateral slip contributions and captures axle-specific wear behaviour. The model is calibrated using real vehicle measurement data and extends existing slip-based wear formulations. Simulation results demonstrate that vehicles equipped with multiple driven axles—particularly heavy-duty electric vehicles—benefit from cost-aware torque distribution, achieving a more balanced utilization of driveline components. Across different driving cycles, the proposed approach reduces the combined cost of electrical energy consumption and tire wear on average by 2.7% and up to 6% compared to energy-focused control allocation strategies.

INDEX TERMS Battery electric vehicle, control allocation, tire wear, torque distribution, electric axle.

NOMENCLATURE

$T_{\mathrm{w_{kg}}}$	Amount of tire worn particles (kg).
s_x	Longitudinal tyre slip.
s_y	Lateral tyre slip.
w_{T}	Tire width (m).
d_{T}	Tire diameter (m).
D_{T}	Tire rubber density ($\frac{\mathrm{Kg}}{\mathrm{m}^3}$).
$T_{\mathrm{w_{kg,sx}}}$	Tire wear caused due to longitudinal slip (kg).
$n_{\mathrm{w},l}$	Number of tires of axle side l.
C_{t}	Wear cost rate of a single tire (per travelled distance) ($\frac{\mathrm{Euro}}{\mathrm{m}}$).
C_{x}	Tire longitudinal stiffness.
$F_{\mathrm{mw,k}}$	Wheel force coming from k^{th} EM (N).
$F_{\mathrm{mw,k,max}}$	Maximum wheel force limit of the k^{th} EM (N).
$F_{\mathrm{mw,k,min}}$	Minimum wheel force limit of the k^{th} EM (N).
F_{br}	Friction brake force (N).
$F_{\mathrm{br,min}}$	Limit of friction brake force (N).
F_{xw}	Longitudinal tyre force (N).
$r_{m,k}$	Total gear ratio of the gearbox and differential related to k^{th} EM.
$F_{\mathrm{mc,k}}$	Input equivalent force to k^{th} EM (N).
n_{em}	Total number of EMs.
n_{dAxles}	Number of driven axles.
R_w	Wheel effective radius (m).
a_{req}	Longitudinal acceleration request ($\frac{\mathrm{m}}{\mathrm{s}^2}$).
m	Gross combination mass (kg).
v_x	Longitudinal velocity ($\frac{\mathrm{m}}{\mathrm{s}}$).
A_f	Front area of the vehicle (m^2).
c_d	Drag coefficient.
ρ_a	Air density ($\frac{\mathrm{kg}}{\mathrm{m}^3}$).
b_{ij}^m	Fitting curve coefficients of the maximum and minimum EM torques.

α	Road grade (positive downhill) (rad).
f_r	Rolling resistance coefficient.
g	Gravitational acceleration ($\frac{\mathrm{m}}{s^2}$).
$\eta_{\mathrm{tm,k}}$	Efficiency of EM transmission.
μ	Road friction coefficient.
h_{ij}^{+}	Fitting function coefficients of the positive EM power consumption.
h_{ij}^{-}	Fitting function coefficients of the negative EM power consumption.

I. INTRODUCTION

Tire wear has become one of the main sources of non-exhaust traffic-related particles due to increased adoption of battery electric vehicles (BEVs) [1], [2]. Particles generated from tire wear are primarily composed of microplastics and contribute to pollution when they disperse into the environment [3], [4]. These microplastics can contaminate soil, water and air, posing risks to wildlife and ecosystems [5], [6]. New regulations aim to label tires based on their wear rate and specific applications, and to establish limits on the maximum allowable tire wear [7]. These measures are designed to encourage the production and use of more durable, environmentally friendly tires and ensure compliance with upcoming regulations by avoiding potential fines.

In addition, the economic implications of tire related maintenance in vehicles are also significant. Tire wear on electric passenger vehicles is 20% higher on the corresponding internal combustion engine vehicle [8]. For commercial heavy vehicles using internal combustion engines, the total tire related costs account for approximately 5% of the total cost of ownership [9]. With electrification, these costs are expected to be higher due to increased wear. Moreover, balancing durability of the tire with rolling resistance to reduce overall operational expenses remains a key challenge for manufacturers. Hence, introducing strategies to minimize tire wear offers environmental and economic benefits, and is therefore an important research topic in tire development.

Vehicle dynamics control (VDC) systems have increasingly been explored as a means to influence and potentially reduce tire wear, particularly in electric vehicles, autonomous vehicles, and over-actuated platforms. VDC has been extensively studied using both traditional model-based strategies and, more recently, learning-based approaches. Classical strategies—including rule-based control, PID control, optimal control, and model predictive control—have been widely applied to longitudinal and lateral vehicle dynamics due to their interpretability, stability guarantees, and real-time implementability [10], [11], [12], [13]. More recently, learning-based methods, particularly reinforcement learning and imitation learning, have shown strong capability in handling high-dimensional, non-linear decision-making problems in tasks such as car-following, lane-changing, and integrated highway driving [14], [15], [16], [17]. Despite their effectiveness in regulating overall vehicle motion, most existing VDC strategies focus on supervisory or reference-level control and do not explicitly coordinate individual actuators or incorporate tire–road interaction dynamics that directly influence wear. Consequently, their impact on tire degradation is largely indirect. In contrast, more direct approaches to mitigating tire wear have focused on vehicle-level interventions, including suspension optimization [2], [18], tire design [19], [20], active steering systems [21] and driving behavior optimization [22], [23], which directly alter the mechanical or operational conditions that govern tire wear. While effective at reducing unfavorable operating conditions, these approaches typically do not exploit the additional control authority available in electric vehicles with distributed propulsion systems, motivating research into torque distribution and control allocation strategies that explicitly consider tire wear.

Building on these vehicle-level and supervisory control approaches, wheel torque distribution and control allocation strategies have emerged as effective means of influencing tire wear in electric vehicles equipped with distributed propulsion systems. Zhao et al. [24] demonstrated that minimizing tire slip energy through optimized torque distribution in four-wheel in-wheel-motor-driven electric vehicles can improve energy efficiency while alleviating excessive tire slip. This concept was extended in [25] by explicitly incorporating tire slip energy into the torque allocation problem for four-wheel-drive electric vehicles, showing that appropriate torque redistribution can reduce unnecessary tire excitation without compromising vehicle stability. To address real-time applicability, Guo et al. [26] proposed a fast model predictive control–based torque allocator that balances slip energy reduction with stability constraints, enabling rapid control updates under dynamic driving conditions. While these approaches highlight the potential of slip-energy-aware torque allocation, tire wear reduction is treated only implicitly, as a secondary outcome of reduced slip or energy dissipation, rather than as an explicit control objective with an associated cost or trade-off.

However, tire slip energy alone does not fully capture the mechanisms governing tire wear. Slip energy reflects instantaneous power dissipation at the tire–road interface and is strongly correlated with longitudinal and lateral slip. Tire wear, in contrast, is a cumulative and non-linear process influenced by additional factors such as contact pressure distribution, temperature evolution, tread material properties, and transient load histories [27], [28]. As a result, minimizing slip energy—often in combination with motor energy loss—does not necessarily correspond to minimizing actual tread degradation, particularly under varying road conditions or prolonged driving cycles. Existing torque allocation studies based on slip energy and motor loss [24], [25], [26] rely on the implicit assumption that reduced slip energy leads to reduced wear, without explicitly modeling wear accumulation, its dependence on operating conditions, or its economic impact over time.

Consequently, although tire slip energy provides a convenient and computationally efficient metric for control design, its ability to accurately represent tire wear remains limited. This motivates the need for control allocation formulations

that move beyond implicit wear mitigation and explicitly incorporate tire wear–related objectives or economic trade-offs, particularly for multi-axle distributed-drive electric vehicles operating under diverse and sustained driving conditions. From this perspective, model extensions and parameter calibration serve as enabling components, whereas the primary contribution lies in the explicit formulation of wear-aware control objectives and their integration into the torque allocation problem. Moreover, there remains a lack of comprehensive and integrated approaches that jointly consider vehicle dynamics, driving behaviour, road conditions, and real-world validation when targeting tire wear minimization. To address the highlighted gaps in research, this paper contributes to the research community through the following contributions:

1) *Unified monetary-cost-based control allocation framework:* The primary contribution of this work is the formulation of a mixed-integer control allocation strategy for distributed-drive electric vehicles that jointly optimizes electric energy consumption and tire wear by expressing both objectives in a common monetary unit (e.g., Euro per second or Euro per meter). This unified cost formulation enables explicit and transparent trade-offs between propulsion energy efficiency and tire wear emissions, which is particularly relevant for heavy-duty vehicles with multiple driven axles.
2) *Wear-cost–aware torque and force distribution across axles and wheels:* Building on the unified cost framework, the proposed controller allocates wheel forces and motor torques while implicitly managing tire slip, allowing the prioritization of motors and axles based not only on electrical efficiency but also on the economic cost of tire wear. This extends conventional energy-focused torque allocation strategies by directly embedding wear-related penalties into the control decision.
3) *Empirical tire wear modelling as an enabling component:* To support wear cost estimation within the control framework, an empirical tire wear model is developed that accounts for both longitudinal and lateral slip contributions. This study extends existing slip-based wear modelling [28], [29], which primarily address lateral slip, and is calibrated using real vehicle measurement data to capture axle-specific wear behaviour under practical operating conditions.

Together, these contributions establish a cost-aware control allocation paradigm that shifts the optimization objective from purely energy considerations toward a more comprehensive economic perspective, explicitly accounting for tire wear emissions alongside electrical energy consumption.

II. PROBLEM STATEMENT

During vehicle operation, tires are subject to friction, heat, and mechanical stress, which lead to gradual degradation and wear. The wear of a tire is a complex phenomenon to analyse, involving various factors, such as operating conditions, vehicle configuration, and tire construction including the material used, [30], [31], [32]. Some of the important factors influencing tire wear include:

- Axle load
- Operating temperature
- Inflation pressure
- Lateral tire slip which is dependent on transport application including road roughness, road curvature, vehicle configuration, wheelbase, etc.
- Longitudinal tire slip, its rate, and sliding distance - which depends on the transport application including road roughness, the driving style, acceleration of the vehicle, type of axle (driven/non-driven), braking control strategy, etc.
- Tire rubber material
- Tire tread shape and depth
- Tire size
- Road type
- Vehicle Speed

Among these factors, longitudinal and lateral tire slips are readily controllable during driving and can be managed to reduce tire wear. The longitudinal slip utilization, which is also proportional to the torque generated by the actuators, such as the electric machines (EMs) and friction brakes, directly influences the energy consumption and tire wear. The lateral slip can be influenced by controlling driving path and curvature, for example through steering control [22], [23].

BEVs utilize regenerative braking to recover kinetic energy and improve overall energy efficiency. To maximize energy recovery, modern BEVs employ brake-blending strategies that prioritize regenerative braking on the driven axles, up to the limits imposed by the motor drive system (MDS) and tire-road interaction. While this method enhances range and reduces energy consumption, it also results in increased longitudinal tire slip on the driven wheels—particularly during frequent acceleration and deceleration events. This increase in longitudinal slip contributes significantly to tire wear, especially on driven axles, where electric motors respond quickly and frequently to torque demands. Compared to internal combustion engine (ICE) vehicles, BEVs exhibit higher levels of torque variability and regenerative braking intensity, leading to a noticeable disparity in tire wear patterns. Simulations and experimental data confirm that BEV drive tires experience accelerated degradation under standard driving conditions [33].

Additionally, reduced energy consumption does not always translate to reduced costs. Tire degradation not only affects safety and vehicle dynamics but also represents a significant operational cost. Understanding the underlying mechanisms linking longitudinal slip, torque demand, and tire wear is essential for evaluating the long-term performance and cost implications of BEV operating strategies. Therefore, this research aims to analyse the tire wear characteristics and propose a control strategy to minimize the operational cost of BEVs.

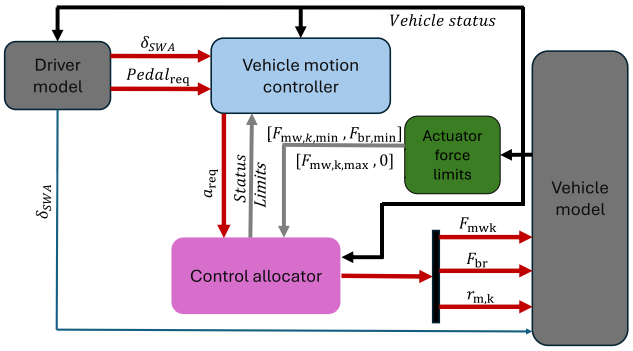

FIGURE 1. Envisioned overview of the implementation using the proposed control allocator.

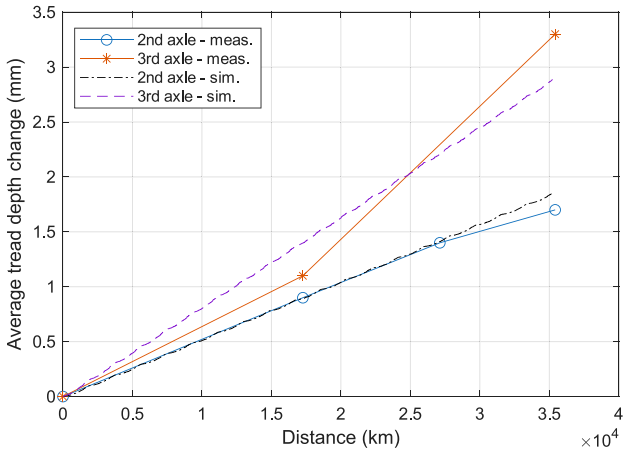

FIGURE 2. Average tire wear tread depth reduction of drive-axles, simulations versus measurements.

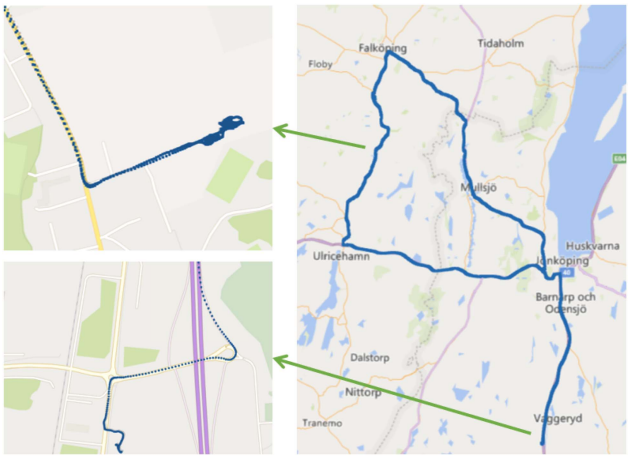

FIGURE 3. The operational environment: regional distribution including warehouses representing driving cycles where tread depth measurements were performed.

III. METHOD

This section summarizes the methods employed in the control allocation problem of minimizing energy consumption along with tire wear. Initially, the tire wear model used in this study is presented along with calibration using real test measurements. Subsequently, the tire wear cost-rate objective is defined, and the resulting optimization-based control allocation problem is formulated.

Fig. 1 illustrates the envisioned control system architecture incorporating a control allocator designed to minimize tire wear and energy consumption. The proposed control allocator receives motion requests from the vehicle motion controller, along with information on actuator operating limits and current vehicle states. To ensure safe operation, constraints and status information associated with the tires and actuators are fed back by the control allocator to the vehicle motion controller.

A. TIRE WEAR MODEL AND EXPERIMENTAL CALIBRATION

A tire wear model, based on the physical principles presented in [28], [29] is used. The wear model is extended in this study to include the effects of lateral slip, longitudinal slip and relation to the vertical load.

The tire wear is modelled by fitting a parabolic function of lateral and longitudinal slips to the measurement data:

$$T_{\mathrm{w_{kg}}} = w_{\mathrm{T}} K_{\mathrm{T}} \int_{s_0}^{s_{\mathrm{f}}} (s_{\mathrm{y}}(s)^2 + s_{\mathrm{x}}(s)^2) ds \tag{1}$$

where, $T_{\mathrm{w_{kg}}}$ is the amount of tire worn particles in Kg, K_{T} is a constant found by experimental calibration, w_{T} is the tire width, and s_0 and s_{f} are vehicle initial and final travelled distance, respectively. The longitudinal slip s_x and lateral slip s_y are obtained as shown in Appendix A.

The tire tread depth reduction dh can be found by

$$dh = \frac{T_{\mathrm{w_{kg}}}}{d_{\mathrm{T}} \pi \, w_{\mathrm{T}} D_{\mathrm{T}}} \tag{2}$$

where d_{T} is the tire diameter, and D_{T} is the tire rubber density. The tread depth measurements has been done on a tractor-semi-trailer, with dimensions as specified in Table 4, for nearly 35000 km covering about three months of driving. The curve fitting was done on all drive-wheels to find a proper value for $K_{\mathrm{T}} = 3.7 \times 10^{-4} \ \frac{\mathrm{Kg}}{\mathrm{m}^2}$. The fitted curves are shown in Fig. 2. The vehicle model described in Appendix A was used together with a simple driver model to accept steering angle and speed profiles from the logged data, to convert it to the inputs given in (26), and then to simulate all the driving cycles within three months of driving. Driving cycles included every manoeuvre the vehicle performed inside warehouses. The simulation output included lateral and longitudinal slips of each axle side of the vehicle. Fig. 3 shows the operational environment of the vehicle between two tread depth measurements. An example of velocity and road wheel steering angle for four days of operations is shown in Fig. 4, illustrating the repetitiveness of operations, and a snapshot of a 10 minutes operation is shown in Fig. 5, illustrating the quality of the model to follow the reference vehicle velocity. Fig. 6 illustrates lateral and longitudinal slips distribution of the left

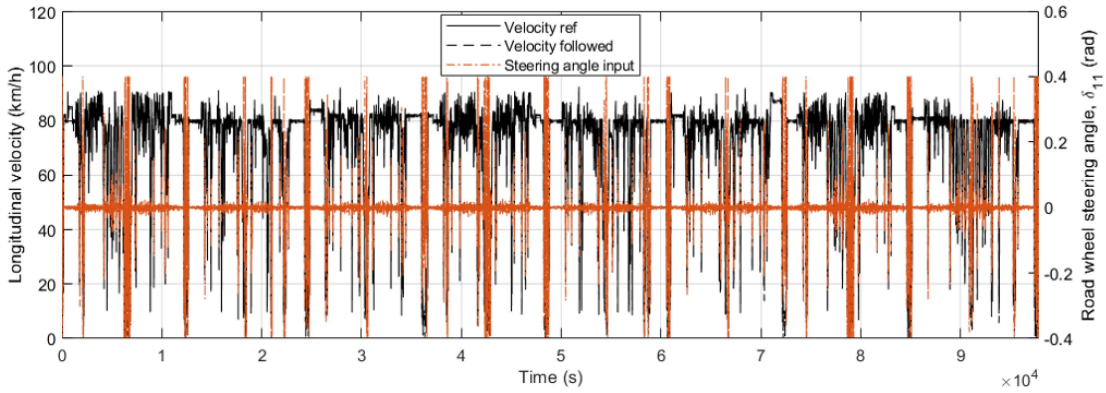

FIGURE 4. Velocity profile and road wheel steering angle of the experimental vehicle of about four days of operations corresponding to Fig. 3.

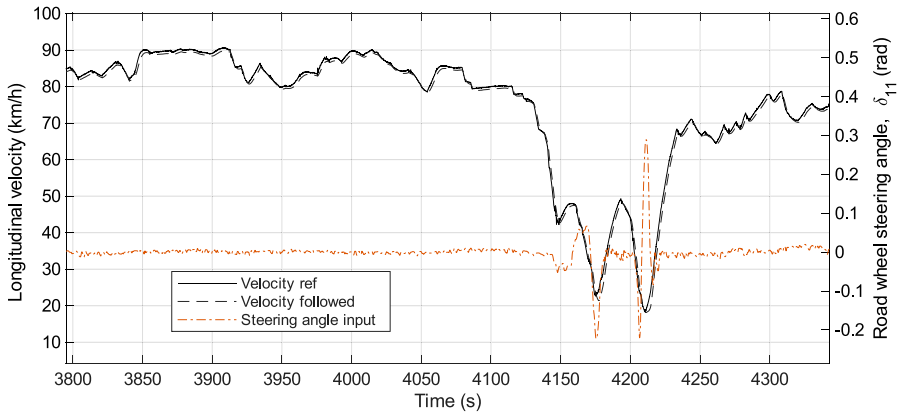

FIGURE 5. Velocity profile and road wheel steering angle of the experimental vehicle of about ten minutes of operations.

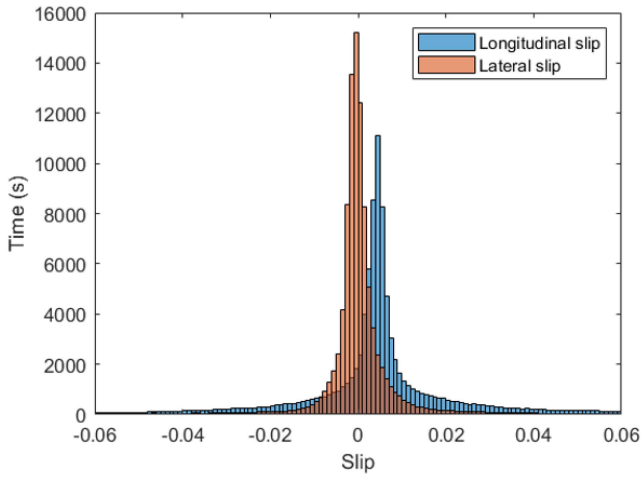

FIGURE 6. Longitudinal slip versus lateral slip distribution of the left wheel of the first driven axle.

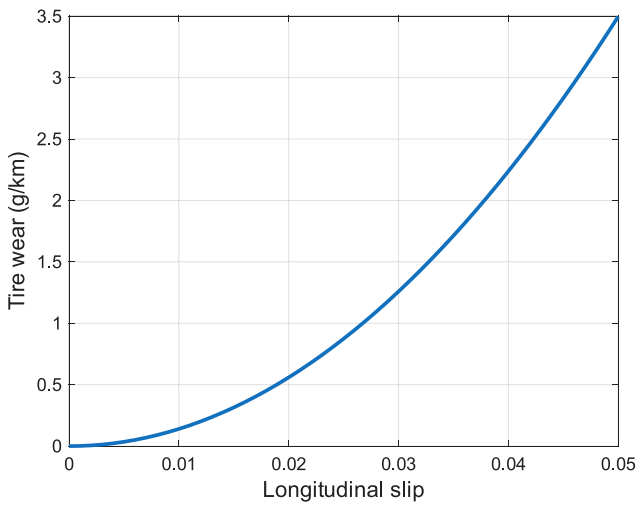

FIGURE 7. Tire wear as a function of longitudinal slip after model calibration for the given tire, vehicle, and operations.

wheel of the first driven axle. The calibrated function relating tire wear to the longitudinal slip is shown in Fig. 7.

B. EVALUATION OF TIRE WEAR COST OBJECTIVE

Lateral slip is not directly controlled in this study because steering-based path optimization is outside the scope of this work. When longitudinal slip stays in the linear range of the tire model, lateral slip is only slightly affected by longitudinal control. However, in sharp turns with high lateral slip, combined-slip tire theory [34], [35], shows that reducing longitudinal slip can also reduce lateral slip while the lateral

TABLE 1. Tire Related Parameters Used in the Control Problem

Parameter	Value
Tire rubber density, D_T ($\frac{\text{Kg}}{\text{m}^3}$)	900
Tire width, w_T (m)	0.378
Electricity price, C_{el} ($\frac{\text{Euro}}{\text{kWh}}$)	0.17
Tire price, p_{t} (Euro)	800
Tire diameter, d_T (m)	0.998

TABLE 2. Metrics on Different Controllers

Control strategy	energy cost*	tire wear cost*	total cost*	% cost reduction
w/o tire wear	0.238	0.033	0.271	0
w tire wear	0.244	0.016	0.260	4

*Unit of cost is Euro/ton/year/10km.

TABLE 3. Parameters of Tire and Vehicle Model Used for Correlation of Test Measurements

Parameter	Value
Gravitational acceleration, g ($\frac{\text{m}}{\text{s}^2}$)	9.81
Product of frontal area, drag coefficient, and air density, $A_{\text{f}}c_{\text{d}}\rho_{\text{a}}$ ($\frac{\text{Ns}^2}{\text{m}^2}$)	9.9840
Rolling resistance coefficient, f_{r}	0.008
Friction ratio, u_2	0.8
Friction ellipse constant, e	1
Maximum lateral force gradient (steered axles), u_{yg}	-0.168
Cornering coefficient at nominal load (steered axles), C_{cy0}	5.33
Maximum lateral force gradient (un-steered axles), u_{yg}	-0.1
Cornering coefficient at nominal load (un-steered axles), C_{cy0}	12.38
Nominal wheel load, F_{z0} (N)	35000
Normalized longitudinal slip stiffness by load at nominal load P_{KX1}	14.848
Modification avoiding singularity, P_{KX2}	-8.0
Exponent in normalized longitudinal slip stiffness by load, P_{KX3}	0.15818
Scale factor of longitudinal slip stiffness, L_{KX}	1
Scale factor of nominal load, L_{FZO}	1

force remains unchanged, (see Fig. 18). Combined-slip tire behaviour is shortly addressed in Appendix B. Direct control of lateral slip would require steering and path optimization, which is not considered here. Therefore, the controller focuses only on longitudinal slip, since it directly contributes to tire wear through propulsion and braking.

Excluding lateral slip and inserting longitudinal slip calculated at zero lateral slip according to (37) into (1) we get tire wear caused by longitudinal slip $T_{\text{w}_{\text{kg,sx}}}$

$$T_{\text{w}_{\text{kg,sx}}} = w_{\text{T}} K_{\text{T}} \int_{s_0}^{s_{\text{f}}} \left(\frac{-F_{\text{xw}}|_{(s_{\text{y}}=0)}}{C_{\text{x}}} \right)^2 ds \tag{3}$$

TABLE 4. Vehicle Configuration and Dimensions

Parameter	Unit 1 (i=1)	Unit 2 (i=2)
m_i (kg)	10250	22000
J_i (kg m^2)	0.4671×10^5	1.6291×10^5
$x_{\text{a}i}$ (m)	[3.12, -1.68, -3.05]	[1.79, -0.91, 0]
$x_{\text{c}i}$ (m)	[0, -4.18]	[7.12, -2.39]
$n_{\text{ta}i}$*	[2, 4, 4]	[4, 4, 0]
μ_i	[1, 1, 1]	[1, 1, 0]

The first vehicle unit has three axles and the other units have two axles. "0" means that either the quantity is not relevant or the axle does not exist.

* n_{ta} denotes the number of tires per axle.

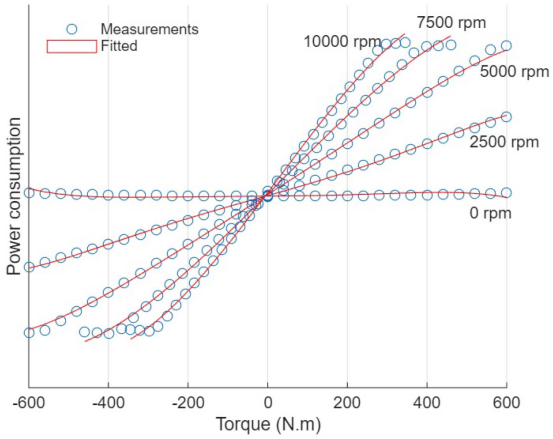

FIGURE 8. Measured power consumption of an EM versus fitted function given in (9).

The tire tread depth reduction dh_{sx} caused by longitudinal slip can be found by

$$dh_{\text{sx}} = \frac{T_{\text{w}_{\text{kg,sx}}}}{d_{\text{T}} \pi w_{\text{T}} D_{\text{T}}} \tag{4}$$

The wear cost rate of a single tire C_{t} (per travelled distance) can be calculated as

$$C_{\text{t}} = \frac{dh_{\text{sx}}}{ds} \frac{p_{\text{T}}}{h} \tag{5}$$

where h is the difference of the tire tread length at the tire beginning and end of life, and p_{T} is the tire price. For an axle side with index l, the cost rate of the tire wear $C_{\text{t},l}$ is then given by

$$C_{\text{t},l} = \frac{dh_{\text{sx}}}{ds} \frac{p_{\text{T}}}{h} n_{\text{w},l} \tag{6}$$

C. CONTROL ALLOCATION INCLUDING TIRE WEAR MINIMIZATION

A mixed-integer non-linear control problem for distributing the propulsion demand of a hybrid or battery-electric heavy vehicle equipped with multiple (n_{em}) EMs, while explicitly accounting for tire wear costs in the cost function, is presented in this study. Including tire wear in the cost function does

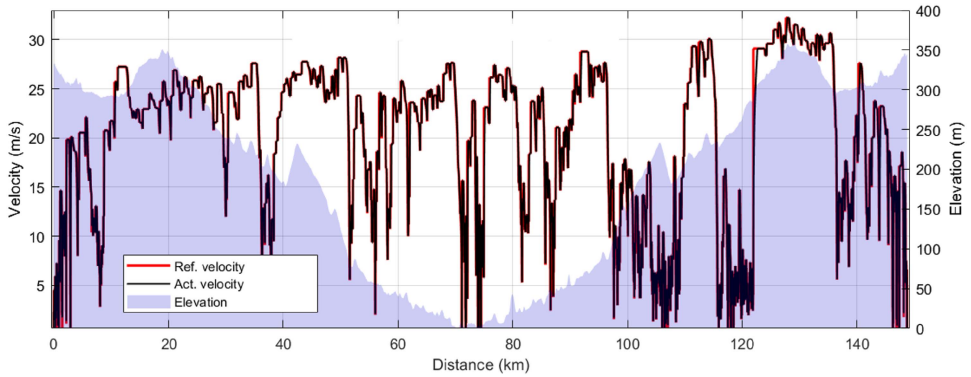

(a) Regional distribution driving cycle.

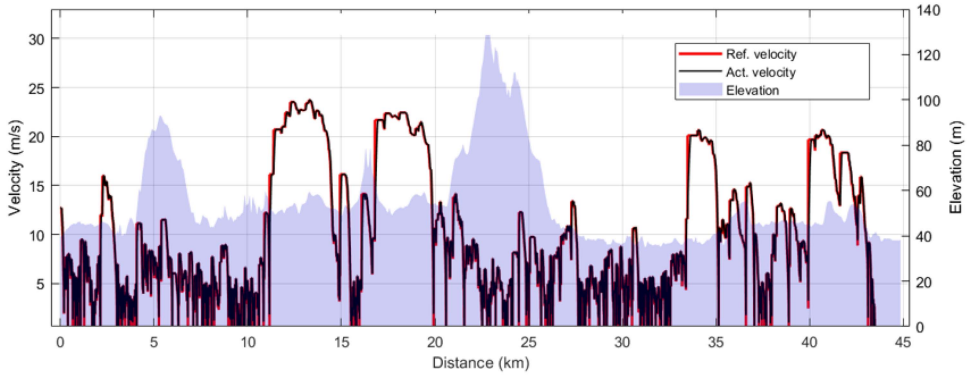

(b) City refuse driving cycle.

FIGURE 9. **Driving cycles.**

not result in additional computational load, because the added cost term is convex.

$$\begin{aligned} &\text{Find} && \{F_{\text{mw,k}}, F_{\text{br}}, r_{m,k} \mid k = 1, \ldots, n_{\text{em}}\} \\ &\text{to minimize} && J = \left(F_{\text{br}} + \sum_{k=1}^{n_{\text{em}}} F_{\text{mc,k}}\right) C_{\text{el}} + \sum_{l=1}^{2 \cdot n_{\text{dAxles}}} C_{\text{t},l} \\ &\text{subject to:} && \end{aligned} \tag{7}$$

vehicle longitudinal dynamics in space domain, road grade α positive downhill:

$$a_{\text{req}} = \frac{1}{m}\Bigg(- F_{\text{br}} + \sum_{k=1}^{n_{\text{em}}} F_{\text{mw,k}} + mg\sin\alpha - mgf_r\cos\alpha - 0.5\rho_a A_f c_d v_x^2\Bigg) \tag{8}$$

EM(s) ($k = 1 \ldots n_{\text{em}}$) power consumption using two 5^{th} degree fitting function for positive and negative torques [36], shown in Fig. 8:

$$F_{\text{mck}} = \begin{cases} \frac{1}{v_x}\sum_{i=0}^{5}\sum_{j=0}^{5} h_{ij,k}^{+}\left(\frac{r_{m,k}}{R_w}v_x\right)^i\left(\frac{R_w F_{\text{mw,k}}}{r_{m,k}\eta_{\text{tm,k}}}\right)^j, \\ F_{\text{mw,k}} > 0 \\ \frac{1}{v_x}\sum_{i=0}^{5}\sum_{j=0}^{5} h_{ij,k}^{-}\left(\frac{r_{m,k}}{R_w}v_x\right)^i\left(\frac{R_w F_{\text{mw,k}}\eta_{\text{tm,k}}}{r_{m,k}}\right)^j, \\ F_{\text{mw,k}} \le 0 \end{cases} \tag{9}$$

EMs torque upper and lower limits ($k = 1 \ldots n_{\text{em}}$) [36]:

$$\begin{aligned} &\frac{R_w F_{\text{mw,k}}}{r_{m,k}\eta_{\text{tm,k}}} - \\ &\min\left\{\sum_{j=0}^{3}\left(\frac{r_{m,k}}{R_w}v_x\right)^j b_{ij,k}^{m}, i = 1, 2\right\} \le 0 \\ &- \frac{R_w F_{\text{mw,k}}\eta_{\text{tm,k}}}{r_{m,k}} + \\ &\max\left\{\sum_{j=0}^{3}\left(\frac{r_{m,k}}{R_w}v_x\right)^j b_{ij,k}^{m}, i = 3, 4\right\} \le 0 \end{aligned} \tag{10}$$

$$\text{where } F_{\text{mw,k,min}} \le F_{\text{mw,k}} \le F_{\text{mw,k,max}} \tag{11}$$

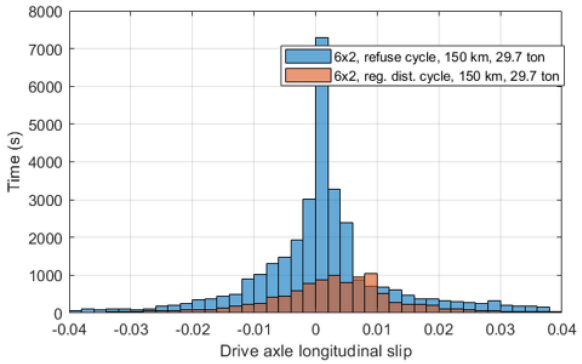

(a) Refuse and regional distribution driving cycles for one axle configuration.

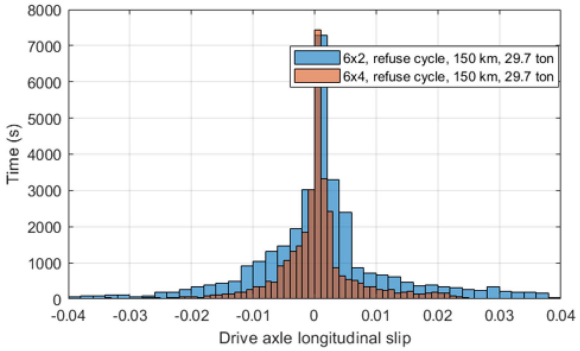

(b) One drive axle longitudinal slip of two vehicles with two different axle configurations.

FIGURE 10. Longitudinal slip distribution.

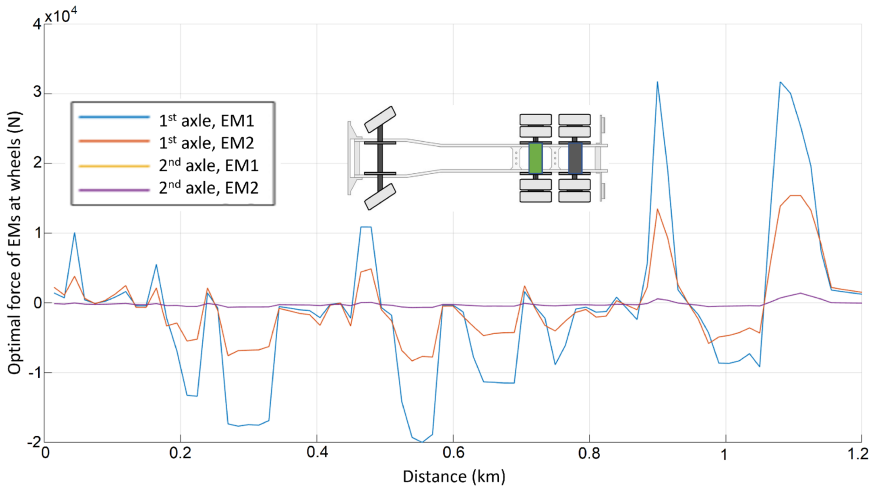

FIGURE 11. The controller performance when the cost function includes energy but it does not account for tire wear. This controller finds optimal energy-efficient power distribution by shutting down the EMs of the second axle.

and, friction brake limits:

$$-F_{\text{br,min}} \leq F_{\text{br}} \leq 0 \tag{12}$$

where decision variables $F_{\text{mw,k}}$, F_{br}, and $r_{m,k}$ are part of the force on wheels that is originated from k^{th} EM, friction brake force on wheels, and gear ratio, including EM off, i.e., when $r_{m,k} = 0$, of k^{th} EM, respectively. The minimum and maximum force limits for $F_{\text{mw,k}}$ are represented by $F_{\text{mw,k,min}}$ and $F_{\text{mw,k,max}}$ respectively and the minimum limit for F_{br} by $F_{\text{br,min}}$. These limits are determined by the actuator force-limits block considering road friction and combined-slip tire behaviour. The cost function is shown in (7), where n_{dAxles} is the number of driven axles and C_{el} is the price of electricity. Likewise, a_{req} is the acceleration request, v_x is the longitudinal speed of the vehicle defined in the constraint equation. The values of the tyre, vehicle and cost rate parameters used in this study are provided in Tables 1 and 3. The problem is solved by sequential programming according to [36]. It should be noted that the problem is not formulated as a model predictive control problem, since it is solved at each time instant with a one-step horizon, which makes it highly computationally efficient.

IV. RESULTS

The results in this section are organized to highlight factors that influence tire slip and, in turn, tire wear, along with differences in controller behaviour when tire wear is included in the cost function versus when it is not. In order to evaluate the performance of optimal control allocator, the controller was tested on a 6x4 tractor for two different driving cycles. This tractor has 3 axles, one front and two rear axles, where the two rear axles are driven. Dimensions are given in Table 4, unit 1. In this paper, each of the driven axles has two EMs, i.e., in total, 4 EMs. Furthermore, the controller's performance, in terms of cost reduction, has been analysed and presented statistically across different driving cycles.

The longitudinal slip of the tires, and consequently tire wear, is influenced by both the driving cycle and the drive-axle

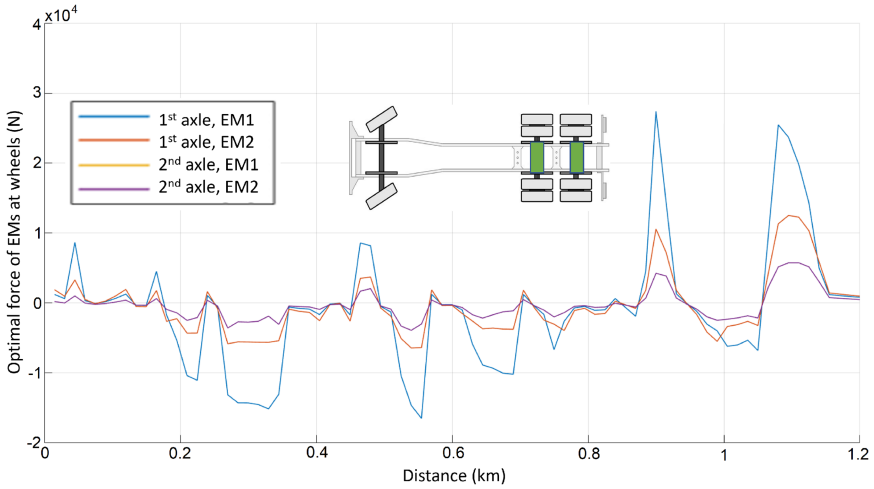

FIGURE 12. The controller performance when the cost function accounts for the cost of energy as well as tire wear for the same cycle as in Fig. 11. This controller finds the optimal cost-efficient power distribution by turning on the EMs of the second axle, where both EMs of the second axle have equal powers.

configuration. To illustrate this effect, Fig. 9(a) and (b) present the regional distribution and city refuse driving cycles, respectively. The main difference between these cycles lies in their speed profiles: the city refuse cycle features more frequent speed changes and a higher number of stops compared with the regional distribution cycle. As a result, the distribution of longitudinal slip differs between the two cycles, as shown in Fig. 10(a), which in turn affects tire wear.

Furthermore, in the city-refuse cycle, vehicles with different numbers of electrically driven axles show varying levels of longitudinal slip and thus experience different rates of tire wear. Fig. 10(b) illustrates the differences in the longitudinal slip distribution for the left wheel of the first driven axle. This variation arises because vehicles with only one driven axle experience higher propulsion and regenerative torques on the driven wheels compared to those with two driven axles.

The performance of two different controllers is shown in Figs. 11 and 12 for the regional distribution driving cycle. In the first controller, the cost function does not include the term that accounts for the cost of tire wear. This controller finds an optimal energy-efficient power distribution by shouting down the EMs of the second driven axle shown in Fig. 11. In the second controller, the cost function includes the term that accounts for the cost of tire wear. This controller finds an optimal cost-efficient power distribution for the same driving cycle where the EMs of the second axle are most often on, as shown in Fig. 12. In this example, both EMs of the second axle have equal powers. Table 2 and Fig. 13 show the cost differences of the controllers in terms of both energy and tire wear. The proposed controller manages to reduce the total cost by about 4% for that driving cycle.

To demonstrate the robustness of the results under diverse driving conditions, approximately 2,300 driving cycles were statistically generated. These cycles differ in terms of road hilliness, speed variations, and vehicle mass, expressed as gross combination weight (GCW). For each driving cycle,

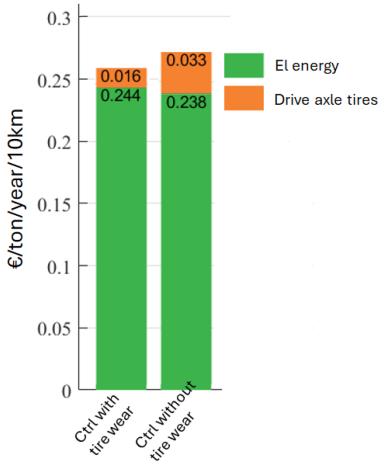

FIGURE 13. The difference between total costs and cost factors as a result of implementing two different controllers. 4% cost reduction is observed when tire wear cost is included in the controller.

the performance of two controllers was evaluated. Fig. 14 presents the probability density of cost reductions achieved by the controller that accounts for tire wear, compared with the controller that considers energy cost only. Furthermore, Fig. 15 illustrates the average cost reduction as a function of road hilliness and different levels of average acceleration. Road hilliness categories—flat (F), predominantly flat (PF), hilly (H), and very hilly (VH)—are defined according to [37]. The average absolute instantaneous acceleration for each driving cycle is computed as follows. Let $\{v_i\}_{i=1}^{N}$ denote the velocity samples and $\{t_i\}_{i=1}^{N}$ the corresponding time samples. The average of the absolute instantaneous acceleration $\bar{a}$ is given by

$$\bar{a} = \frac{1}{N-1} \sum_{i=2}^{N} \left| \frac{v_i - v_{i-1}}{t_i - t_{i-1}} \right|. \tag{13}$$

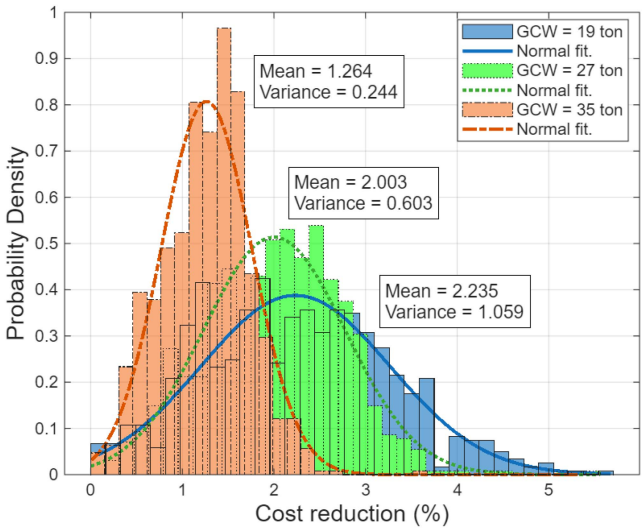

FIGURE 14. Probability density of the cost reduction of a controller with tire wear term over different driving cycles with different road hillinesses and speed variations. Each distribution includes about 750 simulations.

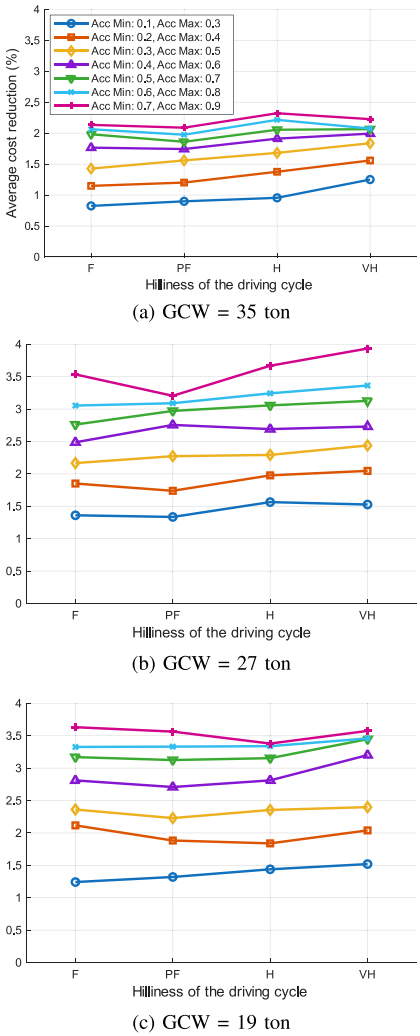

FIGURE 15. Average cost reduction of a controller with tire wear for different GCWs, road hillinesses, and average acceleration given by (13) over the cycle. Different road hillinesses are flat (F), predominantley flat (PF), hilly (H), and very hilly (VH), [37].

V. DISCUSSION

In this paper, it is clearly shown that a control allocation strategy, with and without tire wear cost in the cost function, will change the way total power is distributed between different driven axles. It should be noted that the subject vehicle can have one or more driven axles. If there is only one driven axle, or if there is a possibility to lift the second driven axle and it is lifted, the inclusion of tire wear in the cost function does not affect the controller's action in the case of propulsion. However, in the case of regeneration, the controller may prefer to utilize friction brakes together with the regeneration of the electrically driven axle to reduce tire wear. Reducing tire wear by limiting acceleration could also be implemented, but this is not demonstrated in the controller presented in this paper.

Moreover, the location of the second or additional driven axles is not a limiting factor for the controller. The driven axles could belong to other vehicle units, such as e-dollies and e-trailers. In that case, the controller would still minimize the cost, but additional constraints should be added to account for the stability of the vehicle combination and the torque limits of the electrically propelled units [38].

As highlighted earlier, there are many factors that affect tire wear, but there are not many factors that influence both tire wear and torque distribution, namely longitudinal slip and tire vertical load. Longitudinal slip was directly considered in the controller, but the effect of vertical load is not directly addressed. The effect of vertical load was considered through the non-linear relationship between longitudinal stiffness and vertical load, as shown in (37). The higher the vertical load, the lower the longitudinal stiffness, so a higher slip is needed to provide the same amount of longitudinal force. Therefore, tire wear increases with an increase in vertical load, beside the need for an increase in longitudinal force itself, in case of increased vehicle mass.

Based on the statistical analysis across different driving cycles presented in Figs. 14 and 15, the cost reduction increases for lower GCWs and for higher speed variations, i.e., higher average acceleration. In addition, greater road hilliness leads to a slightly higher cost reduction. The larger cost reduction observed at lower GCWs can be explained by the fact that, under these conditions, the power of a single axle is often sufficient to propel the vehicle for most of the trip. Consequently, the controller that considers only energy cost tends to deactivate one axle to minimize energy consumption. In contrast, the controller that includes tire wear in the cost function prioritizes overall cost minimization and may keep both axles active when this leads to lower combined energy and tire wear costs. At higher GCWs, however, the power provided by a single axle may be insufficient, requiring the energy-only controller to engage both axles more frequently. This inherently reduces tire wear, making the axle power distribution of the controller with the tire wear term more

similar to that of the energy-only controller. As a result, the additional cost reduction achieved by including tire wear is smaller.

Furthermore, increased speed variations and greater road hilliness naturally lead to higher and more variable propulsion demands, providing more opportunities for optimal power distribution between the axles. This, in turn, enables greater overall cost reductions, considering both electricity consumption and tire wear. It should be noted that the reported cost reduction is primarily due to the reduction in tire wear, given the assumed tire price p_t and electricity price C_{el} in Table 1. Moreover, for rangecritical driving cycles, where, for example, the last 2% of the battery's state of charge can determine whether a trip is feasible, the cost term representing tire wear should be neglected or assigned a low weight in order to prioritize energy efficiency over overall cost. In addition, incorporating the tire-wear-related term does not increase the complexity of the control problem. The additional term is a convex function of the control variables; therefore, regardless of the solver used, the computational time of a conventional control allocator remains unchanged compared to a formulation that does not include the tire wear term. Moreover, implementation of the proposed controller on a real vehicle or on a hardware-in-the-loop test platform is left for future work.

Lateral motion control and path planning are also outside the scope of this paper; therefore, neither the steering angle nor lateral slip is treated as an independent control variable. However, in combined manoeuvres involving both longitudinal and lateral slip, the effect of lateral slip is indirectly mitigated through the reduction of longitudinal slip, owing to the combined-slip characteristics of the tire [35]. The proposed controller reduces longitudinal slip by appropriately distributing torque among the driven axles. Consequently, during combined manoeuvres, the lateral slip at each axle is also reduced for a given level of lateral force, which in turn leads to a reduction in tire wear associated with lateral slip.

VI. CONCLUSION

This paper presents an approach to minimize energy consumption and tire wear in battery electric vehicles through an unified monetary-cost-based control allocation framework. This framework incorporates electric energy and tire wear costs while solving an optimization problem. By calibrating a physics-based tire wear model against measurements and integrating it into a control strategy, the paper highlights the critical role of longitudinal slip in influencing tire wear rates. The findings demonstrate that the inclusion of tire wear in the cost function alters the distribution of power among driven axles, leading to reduced operational costs. Moreover, the developed models capture the differences in tire wear rates across various driving cycles and vehicle configurations. The results indicate that vehicles with electric prolusion and particularly with multiple driven axles benefit from a more balanced power distribution, which not only enhances energy efficiency but also mitigates the environmental and economical impact of tire wear.

For future work, the controller should be tested across a broader range of vehicle configurations and ultimately validated in full-scale vehicle experiments. Extending the framework with a wear model that explicitly minimizes both lateral and longitudinal slip would also provide a more robust basis for calibrating tire wear and related performance targets.

APPENDIX A
VEHICLE MODELLING

The paper presents a vehicle model based on Lagrangian dynamics [39], [40], [41], [42], described by non-linear differential algebraic equations (DAEs) or implicit ordinary differential equations (ODEs). The model is formulated in both time and space domains, incorporating generalized coordinates for vehicle position and articulation angles for multi-unit configurations. It includes parameters for tire forces, steering angles, and a non-linear tire model calibrated with real-world data. The model's limitations include ignoring roll, wheel lift, and chassis compliance, assuming moment-free articulation joints, and not accounting for wheel rotational inertia or air resistance on all units. The model's validation used data from normal driving manoeuvres, with options to include lateral load transfer effects in the code. The code and its equations are discussed and experimentally validated in [42]. Here description of the vehicle model used in this study is presented briefly.

Let *ua* and *sa* be binary matrices representing unit wheels and steerable wheels, respectively. For instance, for the two-track 6-axle vehicle shown in Fig. 16:

$$ua = [1, 1, 1, 1, 1, 1; 1, 1, 1, 1, 1, 1],$$
$$sa = [1, 0, 0, 1, 0, 0; 0, 0, 0, 0, 0, 0].$$

Each row in these matrices corresponds to a vehicle unit and its wheels. The number of rows equals the number of units n_u. For example, $ua_{ij} = 1$ and $sa_{ij} = 1$ indicate that unit i has steerable wheel j. The columns represent the maximum number of wheels per unit n_a. The wheels of each unit are numbered from front-right to rear-right and then front-left to rear-left.

The Lagrange equation is formulated as:

$$\frac{d}{dt}\frac{\partial T}{\partial \dot{q}_l} - \frac{\partial T}{\partial q_l} + \frac{\partial V}{\partial q_l} = Q_l, \quad l = 1, \ldots, n_g, \tag{14}$$

where T and V are the kinetic and potential energies of the system, respectively. $n_g = 4$ is the number of generalized coordinates, and the dot () represents a time derivative. The generalized coordinates q are:

$$q = [X_1, Y_1, \phi_1, \theta_1], \tag{15}$$

where X_1 and Y_1 represent the global position of the COG of the first unit. ϕ_1 and θ are the global yaw angle of the first unit and the articulation angles, respectively. The generalized

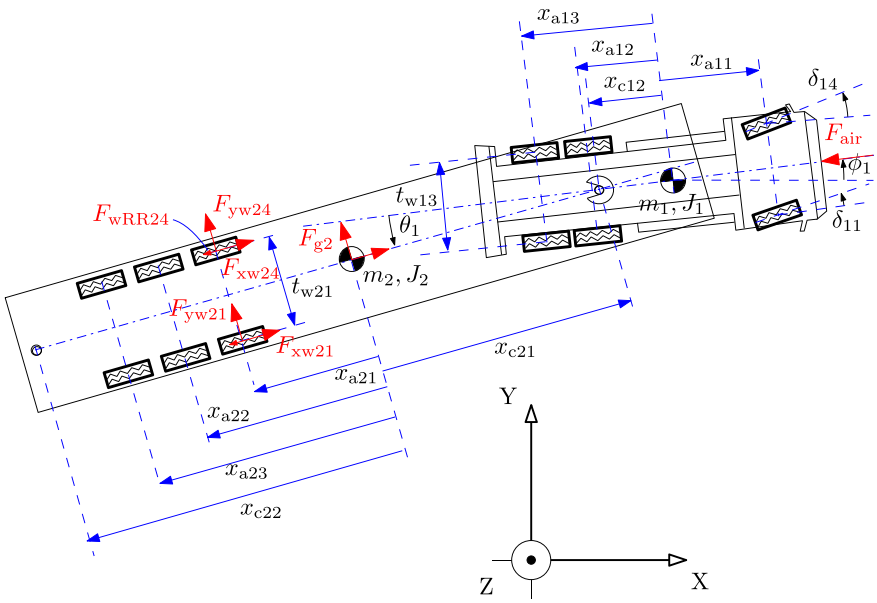

FIGURE 16. Two-track model of a tractor-semitrailer. Forces acting on the vehicle include tire forces F_{xw} from propulsion/braking, tire rolling resistance F_{wRR}, air resistance F_{air}, and body forces on the vehicle's COG due to gravity and road slopes.

force Q_l is defined as:

$$Q_l = \sum_{k=1}^{n_f} \left(F_{Xk} \frac{\partial P_{Xk}}{\partial q_l} + F_{Yk} \frac{\partial P_{Yk}}{\partial q_l} \right), \quad l = 1, \ldots, n_g, \quad (16)$$

where n_f is the total number of force elements. F_{Xk} and F_{Yk} are the X and Y components of the forces, and P_{Xk} and P_{Yk} are their positions in the global inertia frame.

The potential energy is zero, whereas the kinetic energy is given by

$$T = \frac{1}{2} \sum_{i=1}^{n_u} \left(m_i (v_{Xi}^2 + v_{Yi}^2) + J_i \dot{\phi}_i^2 \right), \quad (17)$$

where m_i, J_i, and ϕ_i are the mass, yaw moment of inertia, and yaw angle of the i^{th} vehicle unit, and v_{Xi} and v_{Yi} are the COG velocity components. The potential energy is zero since its affect is captured by the gravitational force.

The positions of the vehicle units' COGs are found using the system kinematics:

$$\begin{bmatrix} X_i \\ Y_i \end{bmatrix} = \begin{bmatrix} X_{i-1} \\ Y_{i-1} \end{bmatrix} + \begin{bmatrix} x_{c(i-1)2} \cos(\phi_{i-1}) - x_{ci1} \cos(\phi_i) \\ x_{c(i-1)2} \sin(\phi_{i-1}) - x_{ci1} \sin(\phi_i) \end{bmatrix}, \quad i = 2, \ldots, n_u, \quad (18)$$

where,

$$\phi_i = \phi_{i-1} + \theta_{i-1}, \quad i = 2, \ldots, n_u, \quad (19)$$

and x_{ci1} and x_{ci2} are the local positions of the front and rear coupling points. For vehicle dimensions, see Fig. 16 and Table 4. Thus, the vehicle unit velocities in the global frame are:

$$v_{Xi} = \frac{dX_i}{dt}, \quad v_{Yi} = \frac{dY_i}{dt}. \quad (20)$$

Consider the matrix M used to convert coordinates from the local frame of a vehicle unit to the global frame:

$$M_i = \begin{bmatrix} \cos(\phi_i) & -\sin(\phi_i) \\ \sin(\phi_i) & \cos(\phi_i) \end{bmatrix}. \quad (21)$$

Using this matrix, the global positions of the wheels X_w and Y_w can be expressed as:

$$\begin{bmatrix} X_{wij} \\ Y_{wij} \end{bmatrix} = \begin{bmatrix} X_i \\ Y_i \end{bmatrix} + M_i \begin{bmatrix} x_{aij} \\ 0 \end{bmatrix}, \quad i = 1, \ldots, n_u, \quad j = 1, \ldots, 2n_a, \quad ua_{ij} \neq 0. \quad (22)$$

The air resistance force position is represented by:

$$\begin{bmatrix} X_{air} \\ Y_{air} \end{bmatrix} = \begin{bmatrix} X_1 \\ Y_1 \end{bmatrix} + M_1 \begin{bmatrix} x_{a11} \\ 0 \end{bmatrix}. \quad (23)$$

As a result, the derived equation of motion forms an implicit system of ordinary differential equations (ODEs):

$$F(x, \dot{x}, u) = 0, \quad (24)$$

where the state vector x is:

$$x = [X_1, Y_1, \phi_1, v_{X1}, v_{Y1}, \dot{\phi}_1, \theta_i, \dot{\theta}_i], \quad i = 1, \ldots, n_u - 1, \quad (25)$$

The input vector u is defined by

$$u = [F_{xwij}, \delta_{11}], \quad i = 1, \ldots, n_u, \quad j = 1, \ldots, 2n_a, \quad ua_{ij} \neq 0. \quad (26)$$

The velocities v_{X1} and v_{Y1} in the state vector (25) are defined in the global frame. We can convert these global frame velocities to the first vehicle unit's local frame using

a coordinate transformation:

$$\begin{bmatrix} v_{x1} \\ v_{y1} \end{bmatrix} = M_1^{-1} \begin{bmatrix} v_{X1} \\ v_{Y1} \end{bmatrix} = \begin{bmatrix} \cos(\phi_1) & \sin(\phi_1) \\ -\sin(\phi_1) & \cos(\phi_1) \end{bmatrix} \begin{bmatrix} \dot{X}_1 \\ \dot{Y}_1 \end{bmatrix}. \quad (27)$$

To differentiate the kinetic energy in (17), we use the chain rule:

$$\begin{aligned} \frac{\partial T}{\partial \dot{X}_1} &= \frac{\partial T}{\partial v_{x1}} \frac{\partial v_{x1}}{\partial \dot{X}_1} + \frac{\partial T}{\partial v_{y1}} \frac{\partial v_{y1}}{\partial \dot{X}_1} \\ &= \frac{\partial T}{\partial v_{x1}} \cos(\phi_1) - \frac{\partial T}{\partial v_{y1}} \sin(\phi_1), \quad (28) \\ \frac{\partial T}{\partial \dot{Y}_1} &= \frac{\partial T}{\partial v_{x1}} \frac{\partial v_{x1}}{\partial \dot{Y}_1} + \frac{\partial T}{\partial v_{y1}} \frac{\partial v_{y1}}{\partial \dot{Y}_1} \\ &= \frac{\partial T}{\partial v_{x1}} \sin(\phi_1) + \frac{\partial T}{\partial v_{y1}} \cos(\phi_1), \quad (29) \\ \frac{\partial T}{\partial \phi_1} &= \frac{\partial T}{\partial v_{x1}} \frac{\partial v_{x1}}{\partial \phi_1} + \frac{\partial T}{\partial v_{y1}} \frac{\partial v_{y1}}{\partial \phi_1} + \frac{\partial T}{\partial g(\phi_1)} \frac{\partial g(\phi_1)}{\partial \phi_1} \\ &= \frac{\partial T}{\partial v_{x1}} v_{y1} - \frac{\partial T}{\partial v_{y1}} v_{x1}, \quad (30) \end{aligned}$$

where $\frac{\partial g(\phi_1)}{\partial \phi_1} = 0$.

The new state set in the first vehicle unit's local coordinate system is:

$$x = [X_1, Y_1, \phi_1, v_{x1}, v_{y1}, \dot{\phi}_1, \theta_i, \dot{\theta}_i], \quad i = 1, \ldots, n_u - 1. \quad (31)$$

To switch from the time domain to the spatial domain, the following variable change can be performed.

$$\frac{d(\cdot)}{dt} = \frac{d(\cdot)}{ds} \frac{ds}{dt} \approx v_{x1} \frac{d(\cdot)}{ds}, \quad (32)$$

and

$$\frac{d^2(\cdot)}{dt^2} = \frac{d}{dt} \left(\frac{d(\cdot)}{ds} \frac{ds}{dt} \right) = v_{x1}^2 \frac{d^2(\cdot)}{ds^2} + v_{x1} \frac{dv_{x1}}{ds} \frac{d(\cdot)}{ds}, \quad (33)$$

where $(\cdot)$ is any variable, assuming $\frac{ds}{dt} \approx v_{x1}$.

1) TIRE MODEL

For simplicity, axle and unit indices are omitted here. We assume a linear longitudinal tire model given by

$$F_{xw}|_{(s_y=0)} = -C_x s_x \quad (34)$$

where $F_{xw}|_{(s_y=0)}$ is the tire longitudinal force in the wheel coordinate system at zero lateral slip s_y, s_x is the tire longitudinal slip, and C_x is the tire longitudinal stiffness which can be tuned based on experimental data [42]. Also, we can assume that C_x is a function of the tire normal force F_z, for instance, for a 315/80R22.5 drive tire, according to tire Magic formula 5.2 [43]:

$$C_x = F_z(P_{KX1} + P_{KX2}\, df_z)\, e^{(P_{KX3}\, df_z)}\, L_{KX}, \quad (35)$$

where,

$$df_z = (F_z - F_{z0}\, L_{FZO})/(F_{z0}\, L_{FZO}), \quad (36)$$

and F_{z0}, P_{KX1}, P_{KX2}, P_{KX3}, L_{KX}, and L_{FZO} are tire parameters according to the tire specification given in Table 3.

According to (26), the inputs to the vehicle model are the wheel longitudinal forces. Therefore, the tire longitudinal slip s_x can be calculated as:

$$s_x = \frac{-F_{xw}|_{(s_y=0)}}{C_x} \quad (37)$$

In order to have an accurate model of vehicle lateral motion, we used a nonlinear lateral tire model in this paper. The tire lateral slip is given by

$$s_y = \frac{v_{wy}}{|v_{wx}|}, \quad (38)$$

The local components of the wheel velocity are:

$$\begin{bmatrix} v_{wx} \\ v_{wy} \end{bmatrix} = \begin{bmatrix} \cos(\phi + \delta) & \sin(\phi + \delta) \\ -\sin(\phi + \delta) & \cos(\phi + \delta) \end{bmatrix} \begin{bmatrix} dX_w/dt \\ dY_w/dt \end{bmatrix}. \quad (39)$$

Therefore, the lateral slip of each tire can be calculated symbolically using the vehicle model. For example, lateral slip of the second axle of the first unit on the right side can be calculated as:

$$\begin{aligned} s_{y12} = \Bigg(& \cos(\phi_1) \Bigg(\cos(\phi_1) v_y + \sin(\phi_1) v_x + \frac{t_{w12} \sin(\phi_1) \dot{\phi}_1}{2} \\ & + x_{a12} \cos(\phi_1) \dot{\phi}_1 \Bigg) - \sin(\phi_1) \Bigg(\cos(\phi_1) v_x - \sin(\phi_1) v_y \\ & - x_{a12} \sin(\phi_1) \dot{\phi}_1 + \frac{t_{w12} \cos(\phi_1) \dot{\phi}_1}{2} \Bigg) \Bigg) \\ & \Bigg| \cos(\phi_1) \Bigg(\cos(\phi_1) v_x - \sin(\phi_1) v_y - x_{a12} \sin(\phi_1) \dot{\phi}_1 \\ & + \frac{t_{w12} \cos(\phi_1) \dot{\phi}_1}{2} \Bigg) + \sin(\phi_1) \Bigg(\cos(\phi_1) v_y + \sin(\phi_1) v_x \\ & + \frac{t_{w12} \sin(\phi_1) \dot{\phi}_1}{2} + x_{a12} \cos(\phi_1) \dot{\phi}_1 \Bigg) \Bigg| \quad (40) \end{aligned}$$

The nonlinear tire model used here is adapted from the Pacejka magic tire model [43]. A revised version of this model [42] is:

$$F_{yw}|_{(s_x=0)} = F_z\, u_y \sin(C \arctan \left(\frac{-C_{cy}}{C\, u_y} \arctan(s_y) \right), \quad (41)$$

where F_z, C_{cy}, and C represent the tire normal force, cornering coefficient, and shape factor, respectively. The shape factor is given by

$$C = 2 \left(1 - \frac{\arcsin(u_2)}{\pi} \right), \quad (42)$$

where $u_2 = \frac{\mu_{slip}}{\mu_{stick}}$ is the ratio between the road friction coefficient at a large slip μ_{slip} and that at a zero slip μ_{stick}, and

$$u_y = 0.8 \left(1 + u_{yg} \frac{F_z - F_{z0}}{F_{z0}} \right), \quad (43)$$

where F_{z0} is the nominal tire normal force, assumed equal to the axle static load, and u_{yg} is the maximum lateral force gradient from -0.3 to -0.1. The cornering coefficient C_{cy} is defined as

$$C_{cy} = C_{cy0}\left(1 - 0.1\frac{F_z - F_{z0}}{F_{z0}}\right); \tag{44}$$

where C_{cy0} is the cornering coefficient at the nominal tire normal force. Values for the maximum lateral force gradient u_{yg} and the cornering coefficient C_{cy0} were tuned using experimental data [42].

Finally, the combined slip was modelled according to the friction ellipse model [34], [42], [43] according to

$$F_{yw} = \sqrt{1 - \left(\frac{F_{xw}}{e\ \mu\ F_z}\right)^2}\ F_{yw}|_{(s_x=0)} \tag{45}$$

where e is a scaling factor defining the shape of the ellipse; e.g., if $e = 1$ the model is a friction circle.

Finally, the tire forces in the global frame can be defined as

$$\begin{bmatrix} F_X \\ F_Y \end{bmatrix} = \begin{bmatrix} \cos(\phi+\delta) & -\sin(\phi+\delta) \\ \sin(\phi+\delta) & \cos(\phi+\delta) \end{bmatrix} \begin{bmatrix} F_{xw} \\ F_{yw} \end{bmatrix},$$

2) OTHER FORCE COMPONENTS

We will consider gravitational forces, rolling resistance forces, and air resistance forces, transforming each to the global frame of reference where necessary. The gravitational force components in the local frame of a unit i are given by:

$$F_{gxi} = m_i\ g\ \sin(\lambda_{pi}), \tag{46}$$

$$F_{gyi} = m_i\ g\ \sin(\lambda_{bi}), \tag{47}$$

where m_i is the mass of unit i, g is the gravitational acceleration, λ_{pi} is the pitch angle, and λ_{bi} is the banking angle positive downhill at the left side of the vehicle unit.

Transform these forces into the global frame using the road yaw angle ϕ_{ri}

$$\begin{bmatrix} F_{gXi} \\ F_{gYi} \end{bmatrix} = \begin{bmatrix} \cos(\phi_{ri}) & -\sin(\phi_{ri}) \\ \sin(\phi_{ri}) & \cos(\phi_{ri}) \end{bmatrix} \begin{bmatrix} F_{gxi} \\ F_{gyi} \end{bmatrix}, \tag{48}$$

where we assumed $\phi_{ri} = \phi_i$.

The rolling resistance force F_{wRR} is expressed as

$$F_{wRR} = -f_r\ F_z\ \frac{v_{x1}}{|v_{x1}|}, \tag{49}$$

where f_r is the rolling resistance coefficient, F_z is the normal force and v_{x1} is the velocity component in the local frame. To transform these forces into the global coordinates, we use:

$$\begin{bmatrix} F_{XRR} \\ F_{YRR} \end{bmatrix} = \begin{bmatrix} \cos(\phi_i+\delta) & -\sin(\phi_i+\delta) \\ \sin(\phi_i+\delta) & \cos(\phi_i+\delta) \end{bmatrix} \begin{bmatrix} F_{wRR} \\ 0 \end{bmatrix},$$

where ϕ_i is the yaw angle, and δ is the steering angle.

The air resistance force is calculated as:

$$F_{xair} = -0.5\ A_f\ c_d\ \rho_a\ v_{x1}^2\ \frac{v_{x1}}{|v_{x1}|}, \tag{50}$$

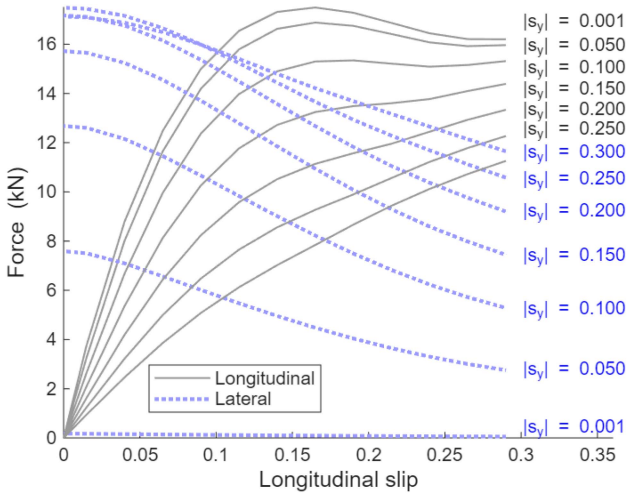

FIGURE 17. Relation between tire lateral and longitudinal forces as a function of lateral and longitudinal slips according to anisotropic tire brush model with a parabolic pressure and stick and slip friction [34]. s_y denotes lateral slip.

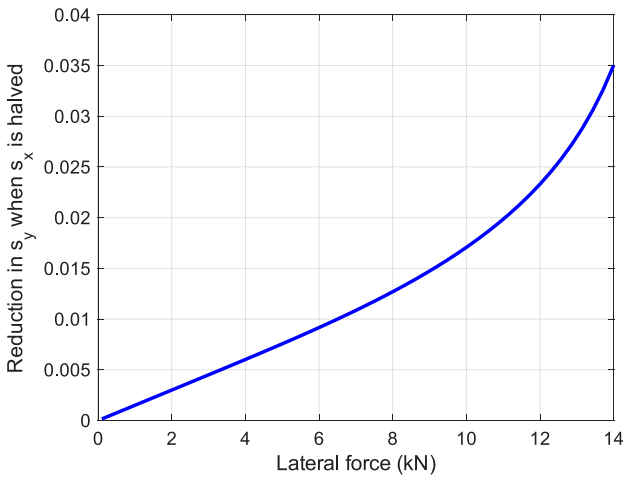

FIGURE 18. Reduction of lateral slip (s_y) when longitudinal slip (s_x) is halved while the lateral force remains unchanged, based on the model given in [34].

$$\begin{bmatrix} F_{Xair} \\ F_{Yair} \end{bmatrix} = \begin{bmatrix} \cos(\phi_1) & -\sin(\phi_1) \\ \sin(\phi_1) & \cos(\phi_1) \end{bmatrix} \begin{bmatrix} F_{xair} \\ 0 \end{bmatrix}, \tag{51}$$

where A_f is the vehicle frontal area, c_d is the air drag coefficient, and ρ_a is the air density.

There are also the effect of lateral load transfer is included in the model. Detailed equations are provided in [42] and [44].

APPENDIX B
COMBINED-SLIP TIRE BEHAVIOUR

Combined-slip tire behaviour has been extensively studied in the literature, and a detailed analysis is beyond the scope of this paper. According to combined-slip theory, an increase in longitudinal and lateral slip leads to a reduction in lateral and longitudinal force, respectively. This behaviour, based on the

anisotropic tire brush model with parabolic pressure distribution and stick–slip friction [34], is illustrated in Fig. 17. Using the same model, Fig. 18 shows the reduction in lateral slip achieved by halving the longitudinal slip while maintaining the same lateral force. This result demonstrates that decreasing longitudinal slip also reduces lateral slip, thereby lowering tire wear associated with it.

Furthermore, as shown in Fig. 17, higher longitudinal slip results in a slower increase in longitudinal force and a faster decrease in lateral force. Consequently, to achieve the same longitudinal force using two driven axles, the required overall longitudinal slip is lower than that of a single driven axle. Similarly, to maintain the same lateral force, the overall lateral slip of two axles is lower than that of a single axle. Experimental validation of the well-established combined-slip tire behaviour is beyond the scope of this work, and interested readers are referred to [45].

REFERENCES

[1] Y. Andersson-Sköld et al., "Microplastics from tyre and road wear: A literature review," Swedish Nat. Road Transport Res. Institute, Linköping, Sweden, VTI Tech. Rep. 1028A, 2020.

[2] G. Papaioannou, J. Jerrelind, and L. Drugge, "A study on skyhook-based suspension control algorithms with regards to tyre wear minimisation in hybrid vehicles," in *Proc. 2021 IEEE Int. Intell. Transp. Syst. Conf.*, 2021, pp. 1643–1649.

[3] K. Pieter Jan, A. Löhr, F. Van Belleghem, and A. Ragas, "Wear and tear of tyres: A stealthy source of microplastics in the environment," *Int. J. Environ. Res. Public Health*, vol. 14, 2017, Art. no. 1265.

[4] F. Sommer et al., "Tire abrasion as a major source of microplastics in the environment," *Aerosol Air Qual. Res.*, vol. 18, no. 8, pp. 2014–2028, 2018, doi: 10.4209/aaqr.2018.03.0099.

[5] T. Grigoratos et al., "Non-exhaust traffic related emissions – Brake and tyre wear PM," Pub. Office Eur. Union, Luxembourg City, Luxembourg, Tech. Rep. EUR 26648, 2014.

[6] K. Magnusson et al., "Swedish sources and pathways for microplastics to the marine environment," IVL Swedish Environmental Research Institute, 2016.

[7] J. Dornoff and F. Rodríguez, "Euro 7: The new emission standard for light- and heavy-duty vehicles in the European union," International Council on Clean Transportation, 2024.

[8] Michelin, "The new demands of EV-cars on tyres and how Michelin has made its tyres EV-suitable," 2023. [Online]. Available: https://news.michelin.se/articles/the-new-demands-of-ev-cars-on-tyres-and-how-michelin-has-made-its-tyres-ev-suitable

[9] Michelin, "How to reduce fleet costs: A guide to optimizing TCO," 2023. [Online]. Available: https://business.michelinman.com/blog/articles/how-to-reduce-fleet-costs-a-guide-to-optimizing-tco

[10] R. Rajamani, *Vehicle Dynamics and Control*, 2nd ed. New York, NY, USA: Springer, 2012.

[11] P. Shi, X. Qian, C. Chadia, Y. Sun, T. Liang, and A. Yang, "A review of research on longitudinal control of intelligent vehicles based on drive/brake by wire," *World Electric Veh. J.*, vol. 15, no. 12, 2024, Art. no. 557. [Online]. Available: https://www.mdpi.com/2032-6653/15/12/557

[12] A. Artuñedo, M. Moreno-Gonzalez, and J. Villagra, "Lateral control for autonomous vehicles: A comparative evaluation," *Annu. Rev. Control*, vol. 57, 2024, Art. no. 100910.

[13] Y. Kebbati, N. Ait-Oufroukh, V. Vigneron, and D. Ichalal, "Coordinated PSO-PID based longitudinal control with LPV-MPC based lateral control for autonomous vehicles," *IEEE Eur. Control Conf. (ECC)*, pp. 518–523, 2022, doi: 10.23919/ECC55457.2022.9838192.

[14] C. Chen, X. Chen, and P. Hang, "Personalized longitudinal motion planning based on a combination of reinforcement learning and imitation learning," *Green Energy Intell. Transp.*, vol. 5, no. 2, 2026, Art. no. 100321. [Online]. Available: https://www.sciencedirect.com/science/article/pii/S2773153725000714

[15] A. Irshayyid, J. Chen, and G. Xiong, "A review on reinforcement learning-based highway autonomous vehicle control," *Green Energy Intell. Transp.*, vol. 3, no. 4, 2024, Art. no. 100156. [Online]. Available: https://www.sciencedirect.com/science/article/pii/S2773153724000082

[16] F. Ye, S. Zhang, P. Wang, and C.-Y. Chan, "A survey of deep reinforcement learning algorithms for motion planning and control of autonomous vehicles," in *Proc. IEEE Intell. Veh. Symp.*, Nagoya, Japan, 2021, pp. 1073–1080.

[17] S. Kuutti, R. Bowden, Y. Jin, P. Barber, and S. Fallah, "A survey of deep learning applications to autonomous vehicle control," *IEEE Trans. Intell. Transp. Syst.*, vol. 22, no. 2, pp. 712–733, Feb. 2021.

[18] J. Schütte and W. Sextro, "Tire wear reduction based on an extended multibody rear Axle model," *Vehicles*, vol. 3, no. 2, pp. 233–256, 2021. [Online]. Available: https://www.mdpi.com/2624-8921/3/2/15

[19] F. Braghin, F. Cheli, S. Melzi, and F. R. and, "Sensitivity analysis of the tyre design parameters with respect to tyre wear using a physical tyre model," *Veh. Syst. Dyn.*, vol. 43, no. sup1, pp. 102–110, 2005, doi: 10.1080/00423110500109034.

[20] C. Liu and D. Cebon, "Modelling wear of truck tyres under high slip," *Veh. Syst. Dyn.*, pp. 1–23, 2025, doi: 10.1080/00423114.2025.2520489.

[21] D. Williams, "Tire wear improvement by steering a third axle," *SAE Int. J. Commercial Veh.*, vol. 4, no. 1, pp. 1–12, 2011, doi: 10.4271/2011-01-2148.

[22] G. Papaioannou, V. Maroof, J. Jerrelind, and L. Drugge, "Optimal control of a long haul automated articulated vehicle for tyre wear minimisation," in *Proc. 2022 IEEE Veh. Power Propulsion Conf.*, 2022, pp. 1–7.

[23] B. D. Steenwyk, E. F. Knuth, N. Mani, and P. Gautam, "Tire cost of ownership relative to vehicle energy cost, route, and tread depth," Bridgestone Americas Inc., Nashville, TN, USA, Tech. Rep. 2021-01-0938, 2021, doi: 10.4271/2021-01-0938.

[24] B. Zhao, N. Xu, H. Chen, K. Guo, and Y. Huang, "Stability control of electric vehicles with in-wheel motors by considering tire slip energy," *Mech. Syst. Signal Process.*, vol. 118, pp. 340–359, 2019. [Online]. Available: https://www.sciencedirect.com/science/article/pii/S0888327018305764

[25] B. Gao, Y. Yan, H. Chu, H. Chen, and N. Xu, "Torque allocation of four-wheel drive EVS considering tire slip energy," *Sci. China Inf. Sci.*, vol. 65, 2022, Art. no. 122202, doi: 10.1007/s11432-019-2946-8.

[26] N. Guo, X. Zhang, Y. Zou, B. Lenzo, T. Zhang, and D. Göhlich, "A fast model predictive control allocation of distributed drive electric vehicles for tire slip energy saving with stability constraints," *Control Eng. Pract.*, vol. 102, 2020, Art. no. 104554. [Online]. Available: https://www.sciencedirect.com/science/article/pii/S0967066120301519

[27] C. Liu and D. Cebon, "Characterizing wear performance of tyre tread rubber," *Wear*, vol. 566-567, 2025, Art. no. 205754. [Online]. Available: https://www.sciencedirect.com/science/article/pii/S0043164825000237

[28] J. Lepine, X. Na, and D. Cebon, "An empirical tire-wear model for heavy-goods vehicles," *Tire Sci. Technol.*, vol. 50, no. 3, pp. 211–229, Jul./Sep. 2022.

[29] C. Liu, "Investigation of severe abrasive truck tyre wear," Ph.D. dissertation, Univ. Cambridge, Apollo - Univ. Cambridge Repository, Cambridge, U.K., 2024, doi: 10.17863/CAM.111100.

[30] A. Sakhnevych and A. Genovese, "Tyre wear model: A fusion of rubber viscoelasticity, road roughness, and thermodynamic state," *Wear*, vol. 542-543, 2024, Art. no. 205291. [Online]. Available: https://www.sciencedirect.com/science/article/pii/S0043164824000565

[31] M. Zhang et al., "A comprehensive review of tyre wear particles: Formation, measurements, properties, and influencing factors," *Atmospheric Environ.*, vol. 297, 2023, Art. no. 119597. [Online]. Available: https://www.sciencedirect.com/science/article/pii/S1352231023000237

[32] O. L. Maıtfe, M. Süssner, and C. Zarak, "Evaluation of tire wear performance," SAE Int., Warrendale, PA, USA, Tech. Rep. 980256, 1998. [Online]. Available: https://saemobilus.sae.org/papers/evaluation-tire-wear-performance-980256

[33] F. Domprobst, "New challenges for tires on battery electric trucks," in *Proc. 18th Int. Symp. Heavy Vehicle Transport & Technol.*, Canada, May 26 to 29, 2025, Art. no. 798. [Online]. Available: https://hvttforum.org/wp-content/uploads/2025/07/798.pdf

[34] B. Jacobson, "Vehicle dynamics compendium; edition 2019," Chalmers Univ., Gothenburg, Sweden, Tech. Rep., 2019. [Online]. Available: https://research.chalmers.se/en/publication/513850
[35] H. B. Pacejka, *Tire and Vehicle Dynamics*, 3rd ed. Oxford, U.K.: Butterworth-Heinemann, 2012.
[36] T. Ghandriz, B. Jacobson, N. Murgovski, P. Nilsson, and L. Laine, "Real-time predictive energy management of hybrid electric heavy vehicles by sequential programming," *IEEE Trans. Veh. Technol.*, vol. 70, no. 5, pp. 4113–4128, May 2021, doi: 10.1109/TVT.2021.3069414.
[37] T. Ghandriz, B. Jacobson, L. Laine, and J. Hellgren, "Impact of automated driving systems on road freight transport and electrified propulsion of heavy vehicles," *Transp. Res. Part C: Emerg. Technol.*, vol. 115, 2020, Art. no. 102610, doi: 10.1016/j.trc.2020.102610.
[38] T. Ghandriz, "Transportation mission-based optimization of heavy combination road vehicles and distributed propulsion, including predictive energy and motion control," Ph.D. dissertation, Chalmers Univ., Göteborg, Sweden, 2020. [Online]. Available: https://research.chalmers.se/en/publication/520358
[39] A. A. Shabana, *Dynamics of Multibody Systems*. Cambridge, U.K.: Cambridge Univ. Press, 2003.
[40] M. Luijten, "Lateral dynamic behaviour of articulated commercial vehicles," Eindhoven Univ., 2010. [Online]. Available: http://www.mate.tue.nl/mate/pdfs/12050.pdf
[41] P. Nilsson and K. Tagesson, "Single-track models of an A-double heavy vehicle combination," Chalmers Univ., Göteborg, Sweden, Tech. Rep. 2013:08, 2014.
[42] T. Ghandriz, B. Jacobson, P. Nilsson, L. Laine, and N. Fröjd, "Computationally efficient nonlinear one- and two-track models for multi-trailer road vehicles," *IEEE Access*, vol. 8, pp. 203854–203875, 2020, doi: 10.1109/ACCESS.2020.3037035.
[43] H. Pacejka, *Tire and Vehicle Dynamics*. Amsterdam, The Netherlands: Elsevier, 2005.
[44] T. Ghandriz, "Multitrailer vehicle simulation: Generation and integration of differential equations," 2020, doi: 10.5281/zenodo.4248263.
[45] F. Bruzelius, M. Hjort, and J. Svendenius, "Validation of a basic combined-slip tyre model for use in friction estimation applications," *Proc. Inst. Mech. Engineers, Part D: J. Automobile Eng.*, vol. 228, pp. 1622–1629, 2014. [Online]. Available: https://api.semanticscholar.org/CorpusID:110640920